International Journal of Nanomedicine

Dovepress
open access to scientific and medical research

Open Access Full Text Article

ORIGINAL RESEARCH

Mesoporous Hollow Manganese Doped Ceria Nanoparticle for Effectively Prevention of Hepatic Ischemia Reperfusion Injury

Peiru Si[1], Jiaxing Lei[1], Chen Yang[1], Peipei Zhang[1], Xiaojiao Li[2], Shaohua Zheng[3], Qingqing Li[1], Jiye Zhang[1]

[1]School of Pharmacy, Health Science Center, Xi'an Jiaotong University, Xi'an, People's Republic of China; [2]Biobank, the First Affiliated Hospital of Xi'an Jiaotong University, Xi'an, People's Republic of China; [3]Department of Anesthesiology, the First Affiliated Hospital of Xi'an Jiaotong University, Xi'an, People's Republic of China

Correspondence: Qingqing Li; Jiye Zhang, School of Pharmacy, Health Science Center, Xi'an Jiaotong University, No. 76 Yanta Westroad, Xi'an, People's Republic of China, Email liqingqing0217@xjtu.edu.cn; zjy2011@xjtu.edu.cn

Introduction: Hepatic ischemia-reperfusion injury (HIRI) is the main reason for liver dysfunction or failure after liver resection and liver transplantation. As excess accumulation of reactive oxygen species (ROS) is the leading factor, ceria nanoparticle, a cyclic reversible antioxidant, is an excellent candidate for HIRI.

Methods: Manganese doped mesoporous hollow ceria nanoparticles (MnO_x-CeO_2 NPs) were prepared, and the physicochemical characteristics, such as particle size, morphology, microstructure, etc. were elucidated. The in vivo safety and liver targeting effect were examined after i.v. injection. The anti-HIRI was determined by a mouse HIRI model.

Results: MnO_x-CeO_2 NPs with 0.40% Mn doped exhibited the strongest ROS-scavenging capability, which may due to the increased specific surface area and surface oxygen concentration. The nanoparticles accumulated in the liver after i.v. injection and exhibited good biocompatibility. In the HIRI mice model, MnO_x-CeO_2 NPs significantly reduced the serum ALT and AST level, decreased the MDA level and increased the SOD level in the liver, prevent pathological damages in the liver.

Conclusion: MnO_x-CeO_2 NPs were successfully prepared and it could significantly inhibit the HIRI after i.v. injection.

Keywords: hepatic ischemia reperfusion injury, Mn-doped mesoporous hollow cerium oxide nanoparticles, oxidative stress

Introduction

Hepatic ischemia reperfusion injury (HIRI) is one of the important complications of liver surgeries, such as liver resection and liver transplantation and it is the main reason for liver dysfunction or failure. Pringle maneuver is commonly used in liver surgeries to interrupt the hepatic blood flow so as to avoid massive bleeding. The ischemic liver gets injured when the blood flow is restored after surgery.[1] Various factors and mechanisms, such as reactive oxygen species (ROS) accumulation, cellular anaerobic metabolism, calcium overload, cytokines over-expression, etc., can lead to hepatocyte injury and death. Among them, the massive accumulation of ROS is generally considered to be the most important factor.[2,3] ROS such as H_2O_2, $\cdot O_2^-$ and ·OH can severely damage the structure and function of the cell via reacting with various cellular components, such as lipids, proteins and nucleic acids. It can also increase the cell permeability via lipid peroxidation,[4] accelerate the cell apoptosis or necrosis.[5]

There is no pharmacological management for HIRI in the clinic. Since ROS is the primary factor for HIRI, antioxidants, which can scavenge ROS has become one of the main research areas for HIRI. Small-molecule antioxidants such as glutathione, vitamin E, resveratrol, edaravone et, al., were reported to attenuate the ischemia-reperfusion injury by removing ROS.[1,6] However, due to the weak anti-oxidant capacity, these small-molecules are easy to be oxidized and exhibit limited efficacy towards HIRI. Therefore, developing pharmacological treatments that can efficiently and persistently scavenge ROS is crucial for the prevention and treatment of HIRI.

Received: 15 December 2022
Accepted: 4 April 2023
Published: 26 April 2023

Graphical Abstract

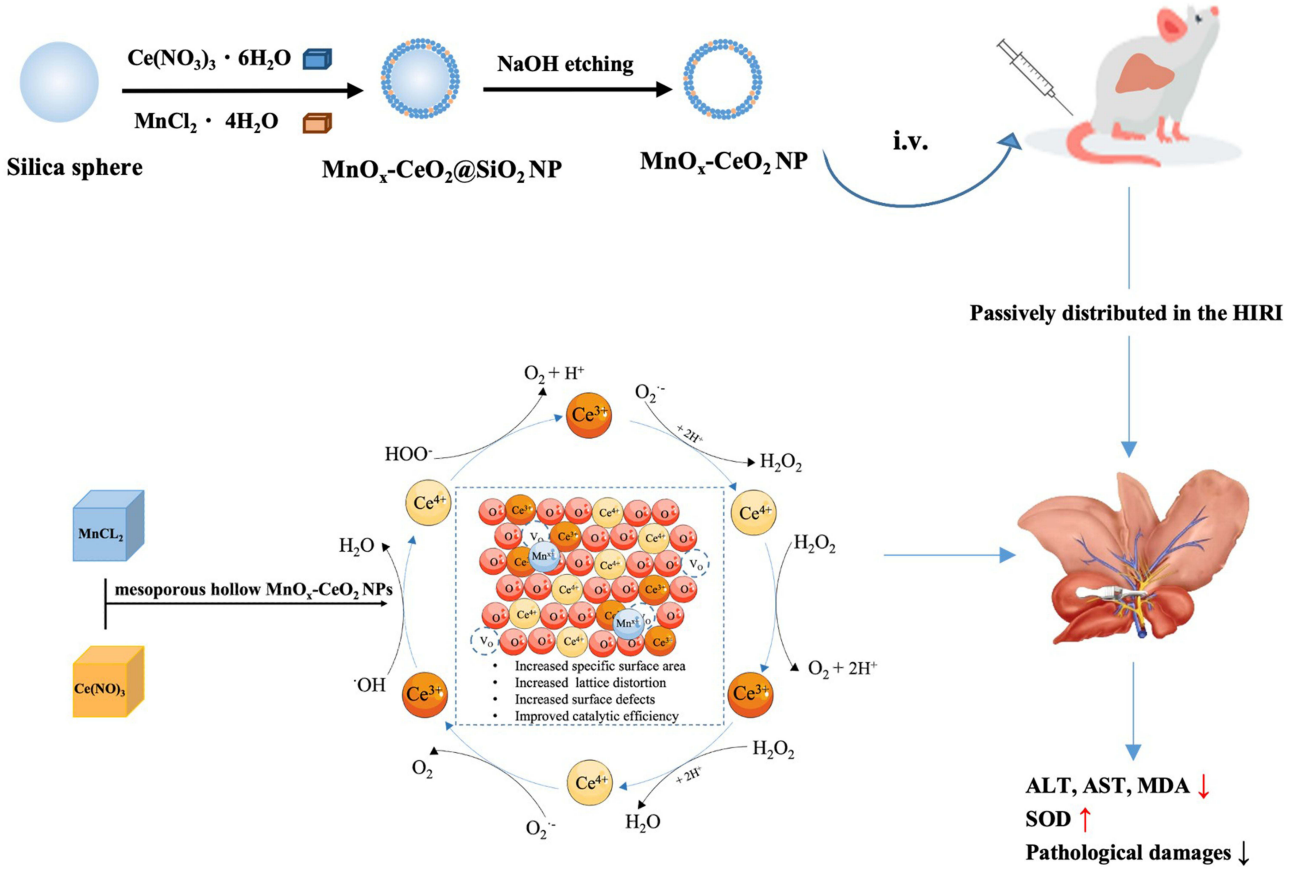

As the Ce^{3+} and Ce^{4+} in nano ceria can reversibly converted to each other, ceria nanoparticles is a novel reversible cyclic antioxidant that can efficiently scavenge various ROS.[7] Due to the excellent anti-oxidant properties of cerium oxide nanoparticles, its inhibitory effect towards stroke,[8] neurodegenerative diseases,[9] acute kidney injury[10] and other ROS-related diseases has been confirmed by many studies.[11] The catalytic efficiency of ceria nanoparticles is closely related with the specific surface area and oxygen vacancy concentration.[12] When the specific surface area gets larger, the coordinated surface atoms are more unsaturated and the surface energy gets higher. Besides, the larger surface area leads to expanded lattice and increased lattice defects, which results in more oxygen vacancies and enhanced catalytic activity. In addition, when other metal elements are doped into nano ceria, the difference in radius and valence between the doping metal ions and cerium leads to lattice distortion and surface defects, which results in a more concentrated oxygen vacancy. Doping with other metal elements, such as Mn, Zr, and Pr, was confirmed to significantly enhance the catalytic efficiency of nano ceria.[13–17] However, whether the improved catalytic efficiency of nano ceria will result in a better in vivo anti-oxidant and anti-HIRI effect still needs to be assured.

In this study, manganese-doped mesoporous hollow ceria nanoparticles (MnO_x-CeO_2 NPs) were synthesized and physiochemically characterized; the relationship between the ROS scavenging efficiency and its structure and composition was clarified; the biodistribution of MnO_x-CeO_2 NPs in mice after intravenous injection was analyzed by ICP-MS; the in vivo anti-HIRI effect of the nanoparticles was evaluated via a mouse HIRI model. Our study represented the first systematic study of applying mesoporous hollow MnO_x-CeO_2 NPs to inhibit HIRI and it will set the stage for further optimization of CeO_2 nanoparticles.

Materials and Methods

Materials

$Ce(NO_3)_3 \cdot 6H_2O$ and DMPO were purchased from Aladdin Biochemical Technology Co., Ltd (Shanghai, China). Methyl violet was bought from Beijing Chemical Industry Group Co., Ltd (Beijing, China). $FeSO_4 \cdot 7H_2O$ was bought from Meryer Co., Ltd (Shanghai, China). TEOS and $MnCl_2.4H_2O$ were purchased from Macklin Biochemical Co., Ltd (Shanghai, China). CheKine^{TM} MDA quantitation kit was bought from Abbkine Scientific Co., Ltd (California, USA). SOD quantitation kit was acquired from Nanjing Jiancheng Biotechnology Co. Ltd (Nanjing, China).

Synthesis of SiO_2 Nanoparticles

48 mL of ethanol, 8 mL of water and 2 mL of ammonia were mixed in a round bottom flask, to which, 5 mL of TEOS and 50 mL of ethanol were subsequently added. After stirring at room temperature for 24 hours, the mixture was centrifuged at 8000 rpm for 10 minutes and the precipitate was washed twice with water and ethanol. Next, the resulted precipitate was dried at 65°C for 6 h to obtain SiO_2 nanoparticles.

Synthesis of SiO_2@MnO_x-CeO_2 Nanoparticles

300 mg of SiO_2 nanoparticles were dispersed in 43 mL of glycol with ultrasonication, to which, 2.25 mL of cerium nitrate and manganese chloride mixed solution was added and stirred for 30 minutes. Next, the mixture was transferred into a high-pressure reactor and incubated in 130°C for 15 hours. After cooling to room temperature, the sample was centrifuged at 12,500 rpm for 10 minutes and the precipitate was washed with ethanol. Next, the resulted precipitate was freeze dried and SiO_2@MnO_x-CeO_2 nanoparticle was obtained. SiO_2@CeO_2 nanoparticles was synthesis with a same method without adding manganese chloride.

Preparation of Mesoporous MnO_X-CeO_2 Nanoparticles

70 mg of SiO_2@MnO_x-CeO_2 nanoparticles were dispersed in 30 mL of H_2O, to which, 1 mL of 2.5 M NaOH was added. Next, the mixture was heated to 50°C and stirred for 2 hours before centrifugation at 3200 rpm for 10 minutes. The precipitate was subsequently washed with water and ethanol before being freeze dried. Mesoporous CeO_2 nanoparticles were prepared with a same method.

·OH Scavenging Effect

The ·OH scavenging effect of MnO_x-CeO_2 nanoparticles with different Mn/Ce ratio was evaluated via a UV-Vis method[18] and an EPR method.[19] In the UV-Vis method, MnO_x-CeO_2 NPs were first dispersed in a 0.1 M Tris-HCl buffer (pH 4.7). Next, a mixed solution which contains 30 μM of methyl violet (MV), 0.15 mM of $FeSO_4$, 100 mM of H_2O_2, 2 $\mu g \cdot mL^{-1}$ or 20 $\mu g \cdot mL^{-1}$ of MnO_x-CeO_2 NP was prepared. The mixed solution was subsequently incubated in 37°C for 1 h before the spectrum at 400–700 nm was measured by a microplate reader (Shanpu, Shanghai, China). In the EPR method, a mixed solution with 2 mM of H_2O_2, 100 mM of DMPO, 0.5 $\mu g \cdot mL^{-1}$ of MnO_x-CeO_2 NP and 1 mM of $FeSO_4$ was prepared, which was immediately transferred into a capillary, and the EPR spectrum was measured and recorded by Electron Paramagnetic Resonance Spectrometer (Bruker, Massachusetts, USA). The mixed solution without MnO_x-CeO_2 NP was considered as the control group.

Physicochemical Characterization

The contents of Ce and Mn in MnO_x-CeO_2 NP was measured by an Inductively Coupled Plasma Mass Spectrometer (NexIONTM 350D, PerkinElmer, Massachusetts, USA). The functional groups on SiO_2 NP, CeO_2 NP and MnO_x-CeO_2 NP were determined by a Fourier transform infrared spectrometer (8400S, Shimadzu, Kyoto, Japan). The crystal structure of SiO_2 NP, CeO_2 NP and MnO_x-CeO_2 NP were tested by an X-ray powder diffractometer (Shimadzu, Kyoto, Japan) after the instrument was calibrated by the monocrystalline silicon powder. The morphology of SiO_2 NP, CeO_2 NP and MnO_x-CeO_2 NP were captured by a transmission electron microscope (H-7650, Hitachi, Tokyo, Japan). The micromorphology and element distribution of CeO_2 NP and MnO_x-CeO_2 NP were observed by a Lorentz

transmission electron microscope (Talos f200x, Thermo Fisher, Massachusetts, USA). The nitrogen adsorption/desorption isotherms of CeO_2 NP and MnO_x-CeO_2 NP were measured by an automatic adsorption instrument (ASAP 2020, micromeritics, Georgia, USA), after which, the specific surface area and pore size distribution were calculated. The molecular structure of CeO_2 NP and MnO_x-CeO_2 NP was analyzed by a Raman spectrometer (DXR2xi, Thermo Fisher, Massachusetts, USA).

Animals

BALB/C mice (male, 20 ± 2 g) were purchased from the Laboratory Animal Service Center of Xi'an Jiaotong University. All animal experiment procedures adhered strictly to the Laboratory animal-Guideline for ethical review of animal welfare and were approved by the Animal Ethical Committee of the Xi'an Jiaotong University (approval number: SCXK (Shaanxi) 2021–341).

Hemolysis Study

5 mL of fresh anticoagulated blood of rat was put in a test tube, which was subsequently centrifuged at 2000 rpm for 10 minutes. The plasma in the upper layer was withdrawn and normal saline was added into the tube to wash the blood cells until the upper layer solution is clear. The red blood cells were obtained after the supernatant was discarded. Next, 1 mL of packed red blood cells were added into 49 mL of normal saline to obtain a 2% (v/v) red blood cell suspension. Different concentrations of MnO_x-CeO_2 NPs (100, 200, 400, 800 μg/mL) in normal saline were added to the 2% red blood cell suspension and incubated at 37°C for 3 h before being centrifuged at 2000 rpm for 10 minutes. The image of the supernatant was taken and the absorbance at 545 nm was measured. The one incubated in normal saline was considered as the negative control and the one incubated in the deionized water was considered as the positive control. The hemolysis rate of the blood cells was calculated according to the following formula:

$$\text{Hemolysis ratio}(\%) = \frac{A_t - A_n}{A_p - A_n} \text{x} 100\%$$

In which, At, An and Ap were the absorbance of the MnO_x-CeO_2 NPs, negative control and positive control.

In vivo Safety Study

Normal saline or different concentrations of MnO_x-CeO_2 NPs (1.25, 2.50, 5.00 $mg \cdot kg^{-1}$) were intravenously injected into the healthy BALB/C mice once a day for two days. The mice were sacrificed 1 day and 28 days after injection before the blood, heart, liver, spleen, lung and kidney were collected. BC-2800vet automatic animal blood cell analyzer (Minray, Shanghai, China) was used to conduct the routine blood analysis. Next, the blood samples were centrifuged at 3000 rpm for 10 minutes before the serum was collected. The level of alanine aminotransferase (ALT) and aspartate aminotransferase (AST) in serum was determined by a biochemical automatic analyzer (Rayto Life Technology, Shenzhen, China). The organs were immersed into 4% paraformaldehyde solution overnight before being embedded in to the paraffin. Next, the organs were sectioned, stained with hematoxylin and eosin for histopathological analysis.

Biodistribution

MnO_x-CeO_2 NPs were injected into the tail vein of BALB/C mice (1 $mg \cdot kg^{-1}$) and the mice were sacrificed 1 hours, 3 hours, 6 hours, and 12 hours later, respectively, before the blood, heart, liver, spleen, kidney and lung were collected. Next, the blood and organs were digested with a mixed solution of nitric acid and hydrogen peroxide (3:1) before the Ce content was detected by ICP-MS (PerkinElmer, Massachusetts, USA).

In vivo Anti-HIRI Study

Mouse HIRI Model Establishment

Fifty BALB/C mice were randomly divided into the following 5 groups (10 mice/group): sham group, HIRI + saline group, HIRI + MnO_x-CeO_2 NP treatment group (0.25, 0.50, 1.00 $mg \cdot kg^{-1}$). MnO_x-CeO_2 NPs or normal saline were intravenously injected into the mice one day and 1 hour before the surgery, respectively. Next, a mouse HIRI model was

built based on a method reported before.[20] Briefly, the mouse was anesthetized with intraperitoneal injection of 1.5% sodium pentobarbital (30 $mg \cdot kg^{-1}$) before the abdomen was open via cutting a 1.5 cm incision along the midline of the abdomen to make the liver exposed. The left hepatic artery, left hepatic duct and portal vein were subsequently occluded with an atraumatic hemostatic clamp. The pale left and middle liver lobes indicate partial liver ischemia. 1 hour later, the left and middle liver lobes turned red after the atraumatic hemostatic clamp was removed, which indicated the blood reperfusion. The abdominal incision was sutured layer by layer and the mouse was kept at 37°C on a heating blanket. 6 hours later, the mouse was sacrificed before the blood and liver were collected. In the sham group, only abdominal incision and suture were performed without blocking the blood flow of the liver.

ALT and AST Level in the Serum

The liver function was assessed by detecting the ALT and AST levels in the serum by a biochemical automatic analyzer (Rayto Life Technology, Shenzhen, China).

Oxidative Stress Levels in Liver

The MDA and SOD levels in the liver were detected by using a lipid peroxidation (malondialdehyde) assay kit and a superoxide dismutase (SOD) assay kit based on the manufacturer's instructions.

Histopathological Analysis

The liver was fixed in 4% paraformaldehyde solution overnight before being embedded in to the paraffin. Next, the organs were sectioned, stained with hematoxylin and eosin for histopathological analysis.[21]

Statistical Analysis

All experiments were conducted in at least triplicate and results were presented as mean ± standard deviations (SD). Two-tailed Student's t tests and ANOVA were used to compare differences among different groups and $p < 0.05$ was considered to be statistically significant.

Results and Discussion

The Influence of Mn Doping Ratio on the ·OH Scavenging Ability of MnO_x-CeO_2 NPs

The MnO_x-CeO_2 NPs was synthesized via depositing MnO_x and CeO_2 on the surface of the Si nanoparticle, in which the Si nanoparticle served as a mesoporous frame. As the oxygen vacancy concentration was reported to be increased when Mn was doped into nano ceria with a doping ratio within 40%,[22] therefore, MnO_x-CeO_2 NPs with different Mn doping ratios were prepared and the actual Mn% in the nanoparticles were investigated via ICP-MS. As shown in Table S1, the Mn% increased as the amount of Mn added increased. However, the actual Mn% was only 4.4% when 40% $MnCl_2$ were added in the synthesis process. The effect of doping ratio on the anti-oxidant properties was investigated with an anti-methyl violet fading test and an EPR measurement so as to optimize the MnO_x-CeO_2 NPs. In the anti-methyl violet fading test, Fe^{2+} catalyzed H_2O_2 to generate hydroxyl radicals, which attacked the double bond of methyl violet (MV) and made it fade. Therefore, the low absorbance indicated the existence of large amounts of hydroxyl radicals in the system, which correlated well with our result (Figures 1 and S1). After being incubated for 1 h, the absorbance of H_2O_2 group was much lower than that of the H_2O group. When MnO_x-CeO_2 NPs were added, the absorbance was significantly increased, which indicated the MnO_x-CeO_2 NPs could scavenge hydroxyl radicals and thereby protect MVs from fading. Next, the hydroxyl radical scavenging effect of CeO_2 NPs and MnO_x-CeO_2 NPs with different doping ratio were compared. As exhibited in Figure 1A, MnO_x-CeO_2 NPs with a Mn doping ratio of 4.00% exhibited the highest absorbance, which indicated that MnO_x-CeO_2 NPs with a Mn doping ratio of 4.00% exhibited the highest hydroxyl radical-scavenging effect.

An EPR measurement was also used to verify the hydroxyl radical scavenging ability of different MnO_x-CeO_2 NPs. As shown in Figure 1B, the multiple peaks with a height ratio of 1:2:2:1 are typical hydroxyl radical signals, whose intensity are highly sensitive to the amount of hydroxyl radicals. In the group with only H_2O_2 and $FeSO_4$, strong EPR signals could be observed. However, when 0.5 $\mu g \cdot mL^{-1}$ CeO_2 NP or MnO_x-CeO_2 NP were added, the EPR signals were significantly weakened and the EPR signals in MnO_x-CeO_2 NP (4.00%) group exhibited the lowest amplitude. This result

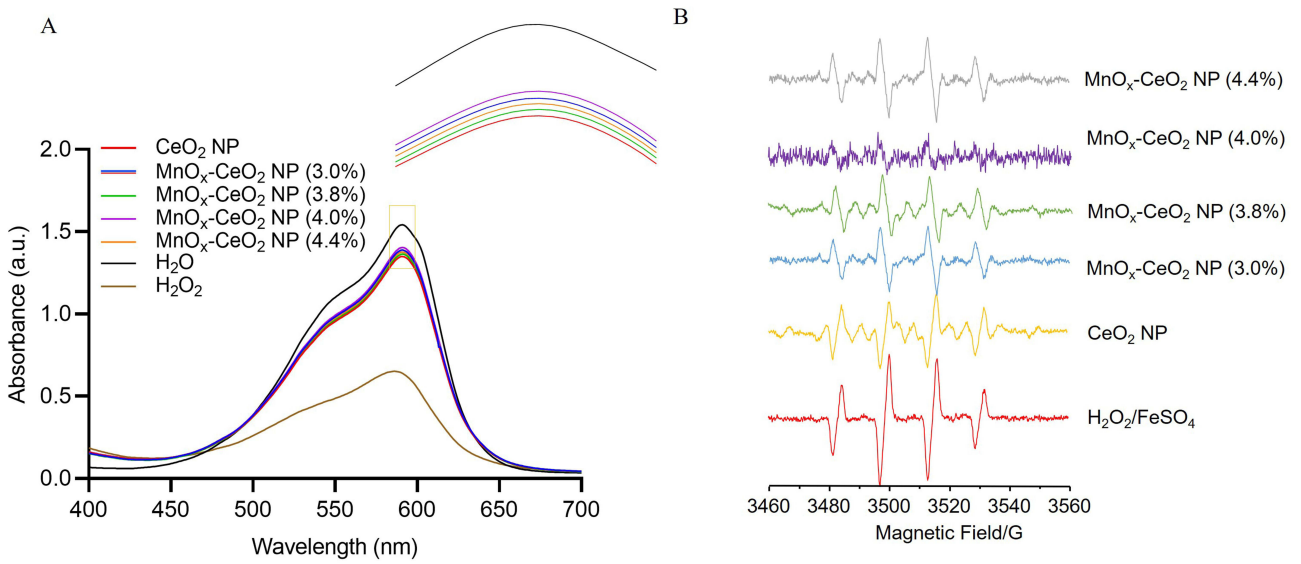

Figure 1 The influence of Mn doping ratio on the hydroxyl radical scavenging ability of MnO_x-CeO_2 NPs. (**A**) anti-methyl violet fading test, (**B**) EPR test.

indicated that both CeO_2 NPs or MnO_x-CeO_2 NPs exhibited good antioxidant capacity, among them, MnO_x-CeO_2 NP with a 4.00% Mn doping ratio exhibited the strongest hydroxyl radical-scavenging capability. This result correlated well with the anti-methyl violet fading test. Therefore, in this study, MnO_x-CeO_2 NP with a 4.00% Mn doping ratio was selected, its physicochemical characteristics and therapeutic effect on HIRI was further investigated.

Physicochemical Characterization of MnO_x-CeO_2 NPs

The particle size and morphology of MnO_x-CeO_2 NPs were investigated via TEM and HRTEM. As shown in Figures 2 and S2, SiO_2 NPs were solid spherical nanoparticles with smooth surfaces and the diameter was about 160 nm. While SiO_2@MnO_x-CeO_2 NPs and SiO_2@CeO_2 NPs are solid spheres with rough surfaces, MnO_x-CeO_2 NPs and CeO_2 NPs are mesoporous hollow spheres with rough surfaces. The particle size of MnO_x-CeO_2 NPs and CeO_2 NPs was about 220 nm, and the deposit layer of both nanoparticles were about 20 nm. Lattice fringes were observed on the surface of SiO_2@MnO_x-CeO_2 NPs, MnO_x-CeO_2 NPs and CeO_2 NPs, the lattice spacing in these nanoparticles was 0.310 nm, 0.310 nm and 0.313 nm, respectively, which represent the standard lattice spacing of the (111) crystal plane of the cubic CeO_2.[23] The smaller lattice spacing in SiO_2@MnO_x-CeO_2 NP and MnO_x-CeO_2 NP may be related to the decreased crystallinity resulted from Mn doping. In addition, the intensity of diffraction rings in the SAED (selected area electron diffraction) pattern of MnO_x-CeO_2 NPs was much lower than that of SiO_2@MnO_x-CeO_2 NP, the (111), (220) and (311) crystal planes corresponded to the cubic CeO_2. In the EDX (energy dispersive X-ray spectroscopy) image of SiO_2@MnO_x-CeO_2 NP, Si was observed to be distributed evenly in the center, Ce and Mn mainly distributed on the surface, O was distributed in both center and surface. Therefore, Ce and Mn were deposited on the surface of SiO_2 in the form of MnO_x and CeO_2. No obvious two-phase separation (separated cerium oxide or manganese oxide) could be observed, which indicated the formation of a solid solution of manganese doped-cerium oxide. In the EDX diagram of MnO_x-CeO_2 NPs, Ce, Mn, O and Si were observed in the hollow spheres, which implied the combination of Si and Ce/Mn or the SiO_2 wat not fully eroded by NaOH. In the EDX image of CeO_2 NPs, Ce, O and Si could be observed.

The crystalline structure of the nanoparticles was detected by XRD. The 2 Theta angle of the SiO_2 NP diffraction peak is 21.8°, corresponding to the (111) crystal plane of SiO_2, and the 2 Theta angle of the CeO_2 NP diffraction peak was 28.5°, 33.1°, 47.5°, 56.4°, and 76.6°, respectively, corresponding to the (111), (200), (220), (311) and (331) crystal planes of cubic CeO_2. No Mn_xO_y related crystal planes were detected in MnO_x-CeO_2 NPs, indicating that Mn^{x+} may entered the CeO_2 lattice and formed a stable solid solution. Besides, the (111) crystal plane of SiO_2 with weak diffraction intensity could also be observed, implying the presence of SiO_2, which was consistent with the EDX results.

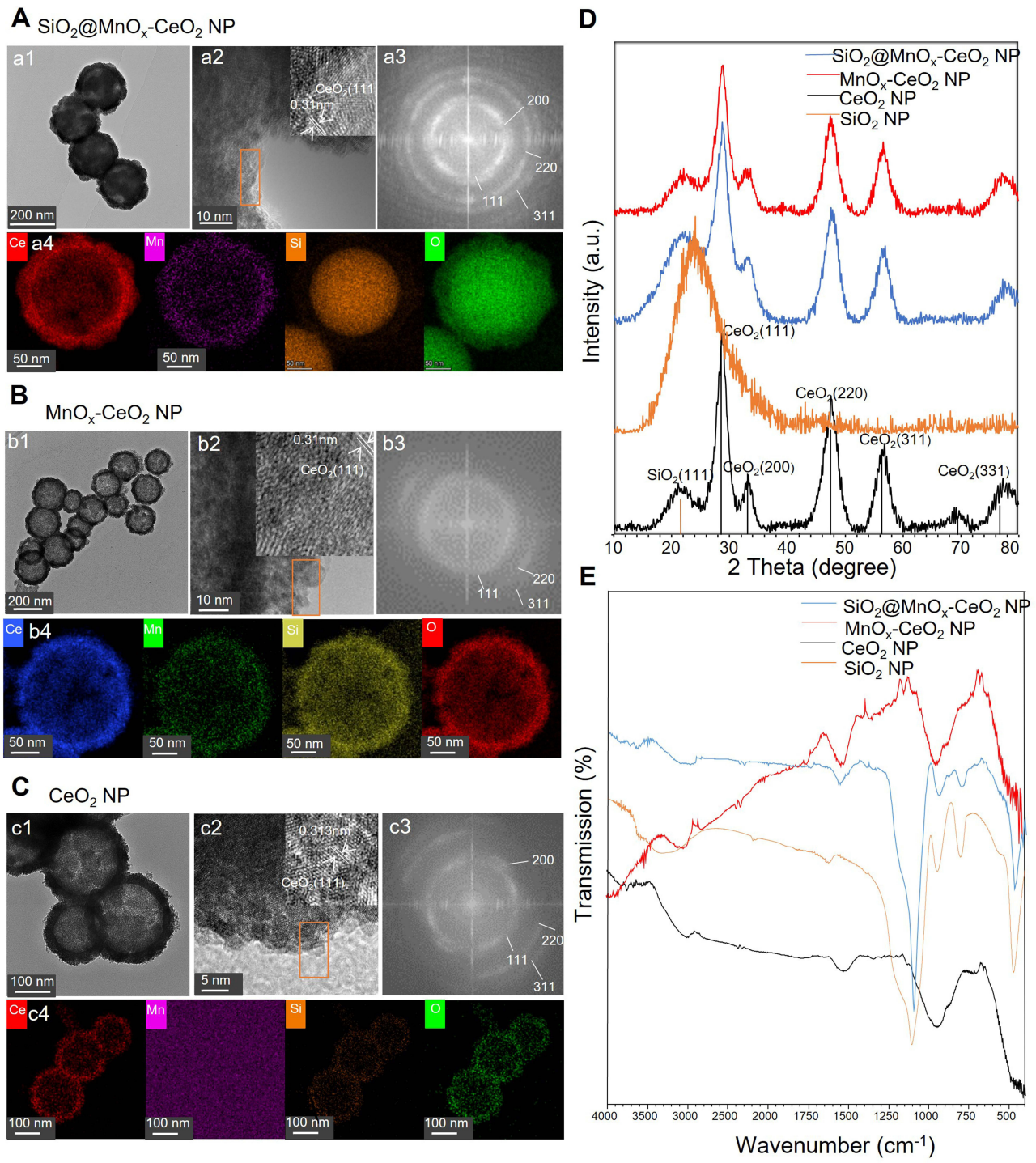

Figure 2 Physicochemical characterization of different nanoparticles. (**A**) The micromorphology of SiO_2@MnO_x-CeO_2 NPs, a1 and a2: HRTEM image, upper right was a further enlarged image of the Orange rectangle part, a3: SAED mode image, a4: energy dispersive X-ray energy spectrum image. (**B**) The micromorphology of MnO_x-CeO_2 NPs, b1 and b2: HRTEM image, upper right was a further enlarged image of the Orange rectangle part, b3: SAED mode image, b4: energy dispersive X-ray energy spectrum image. (**C**) The micromorphology of CeO_2 NPs, c1 and c2: HRTEM image, upper right was a further enlarged image of the Orange rectangle part, c3: SAED mode image, c4: energy dispersive X-ray energy spectrum image. (**D**) Infrared spectrum. (**E**) X-ray diffraction spectrum.

Next, FTIR spectroscopy was used to determine the functional groups on the surface of nanoparticles. In SiO_2 NPs, the broad absorption of hydroxyl and H-bonded silanol groups from 3600 cm^{-1} to 2650 cm^{-1}, the absorption of hydroxyl group at 1630 cm^{-1}, the absorption of Si-O-Si at 1050 cm^{-1} and 790 cm^{-1} and the characteristic absorption of Si-O- at 950 cm^{-1} were observed. In SiO_2@MnO_x-CeO_2 NPs, the intensity of characteristic absorption peak of hydroxyl and

H-bonded silanol groups from 3600 cm^{-1} to 2650 cm^{-1} were weakened and absorption peaks of Si-O-Si and Si-O- still exist, which proved the existence of SiO_2. In MnO_x-CeO_2 NPs and CeO_2 NPs, the Si-O-Si absorption peaks were greatly weakened and the Si-O- characteristic absorption peak still could be observed, which indicated that SiO_2 was greatly corroded by NaOH.

XPS was used to analyze the element composition of the nanoparticles and the valence state of different elements was analyzed, in which C 1s orbital binding energy (284.8 eV) was used as a reference to correct the binding energy of other elements. As shown in Figure 3A and B, the 3d 5/2 and 3d 3/2 spin orbits in Ce 3d were marked as v and u,[24] respectively. Among them, v, v´´, v´´´, u, u´´, u´´´ were characteristic peaks of Ce^{4+}; v_0, v´, u_0 and u´ were characteristic peaks of Ce^{3+}. This confirmed the coexistence of Ce^{4+} and Ce^{3+} in CeO_2 NPs and MnO_x-CeO_2 NPs. By integrating the peak areas of Ce^{3+} and Ce^{4+}, the proportion of the two cations were obtained and the percentage of Ce^{3+} in MnO_x-CeO_2 NPs and CeO_2 NPs was 21.4% and 23.7%, respectively, which did not decrease significantly after CeO_2 NPs were doped with Mn. There was a broad peak containing two shoulder peaks (526.0~534.0 eV) in O 1s spectrum. Through peak-differentiating and imitating, lattice oxygen species (528.9~529.5 eV, Oβ) and surface oxygen species (531.0~531.5 eV, Oα) were obtained.[25] The proportions of Oα and Oβ in MnO_x-CeO_2 NPs and CeO_2 NPs were shown in Table 1. The surface oxygen species (Oα) were reported to be more active than the lattice oxygen species (Oβ), owing to the higher mobility. The proportions of Oα increased significantly after Mn were doped. Compared with CeO_2 NPs, the binding energy of Oα and Oβ peaks of MnO_x-CeO_2 NPs shifted to lower values, which was a result of the chemical atmosphere change of O after Mn doping. There were mainly 2p 3/2 and 2p 1/2 orbits in Mn spectrogram, however, the peak intensity was too low to acquire an accurate result after peak-differentiating and imitating.

Both the CeO_2 NPs and MnO_x-CeO_2 NPs exhibited a type IV isotherm with H1-type hysteresis (Figure 3C), which indicated the existence of mesoporous structure in the nanoparticles.[26] Bimodal pore size distribution was found in MnO_x-CeO_2 NPs (Figure 3D). As shown in Table 1, the specific surface area of MnO_x-CeO_2 NPs was about 245.42 $m^2 \cdot g^{-1}$, which was significantly higher than that of CeO_2 NPs (117.68 $m^2 \cdot g^{-1}$). Therefore, after doping with Mn, the specific surface area and the pore volume of the CeO_2 NPs was significantly increased and this result correlated well with the improved ROS-scavenging effect of MnO_x-CeO_2 NPs.

Raman spectroscopy was used to detect the change of oxygen species on the surface of the MnO_x-CeO_2 NPs when it was reacted with H_2O_2 and the results are shown in Figure 3E. The Raman shift of MnO_x-CeO_2 NPs was directly related to the aggregation of oxygen species adsorbed on the surface and the defects in adsorption sites.[27] The characteristic vibrational peak (F2g) of cubic fluorite structure typical of ceria-based materials at 465 cm^{-1} was observed in the Raman spectrum of MnO_x-CeO_2 NPs. The F2g peak was related to the symmetrical breathing vibration of the O atom around Ce. The higher F2g peak intensity indicated more ordered lattice structure. After the addition of H_2O_2, the intensity of F2g peak decreased, implying that the symmetrical breathing vibration of the O atom around Ce at the beginning of the reaction was weakened and the arrangement of oxygen lattice structure was disordered. In addition, there were two new peaks (0 minute) at 860 cm^{-1} and 880 cm^{-1} in the Raman spectra of MnO_x-CeO_2 NPs, which was attributed to the surface-adsorbed peroxide species[28] (O_2^{2-}) right after the addition of H_2O_2. Later, the peak at 880 cm^{-1} gradually disappeared and the peak at 860 cm^{-1} was progressively weakened, which indicated the dissociation of O_2^{2-} during the reaction between MnO_x-CeO_2 NPs and H_2O_2. The adsorption and dissociation of O_2^{2-} was considered as an antioxidant cycle and H_2O_2 was added again after one cycle to observe the cyclic catalytic property of the nanoparticles. As shown in Figure 3F, the adsorption and dissociation of O_2^{2-} were also observed in the second and third antioxidant cycles. Therefore, MnO_x-CeO_2 NPs could cyclically catalyze the decomposition of H_2O_2.

The Biocompatibility of the MnO_x-CeO_2 NPs

In the hemolysis study, hemolysis could be observed in the positive control group, but there was no hemolysis in the negative control group and the MnO_x-CeO_2 NPs group (Figure 4A and B). The hemolysis rate of the MnO_x-CeO_2 NPs group was within 5%, indicating that MnO_x-CeO_2 NP was quite safe for injection.

As MnO_x-CeO_2 NPs with a maximum concentration of 500 μg/mL showed no cytotoxicity effect in the LDH assay, the maximum dose in the in vivo toxicity study was calculated by the following formula: 500 μg/mL*0.1 mL/10g=5.0 mg/kg, in which 0.1mL/10g means 0.1 mL nanoparticles was injected in mice with a weight of 10 g. ALT

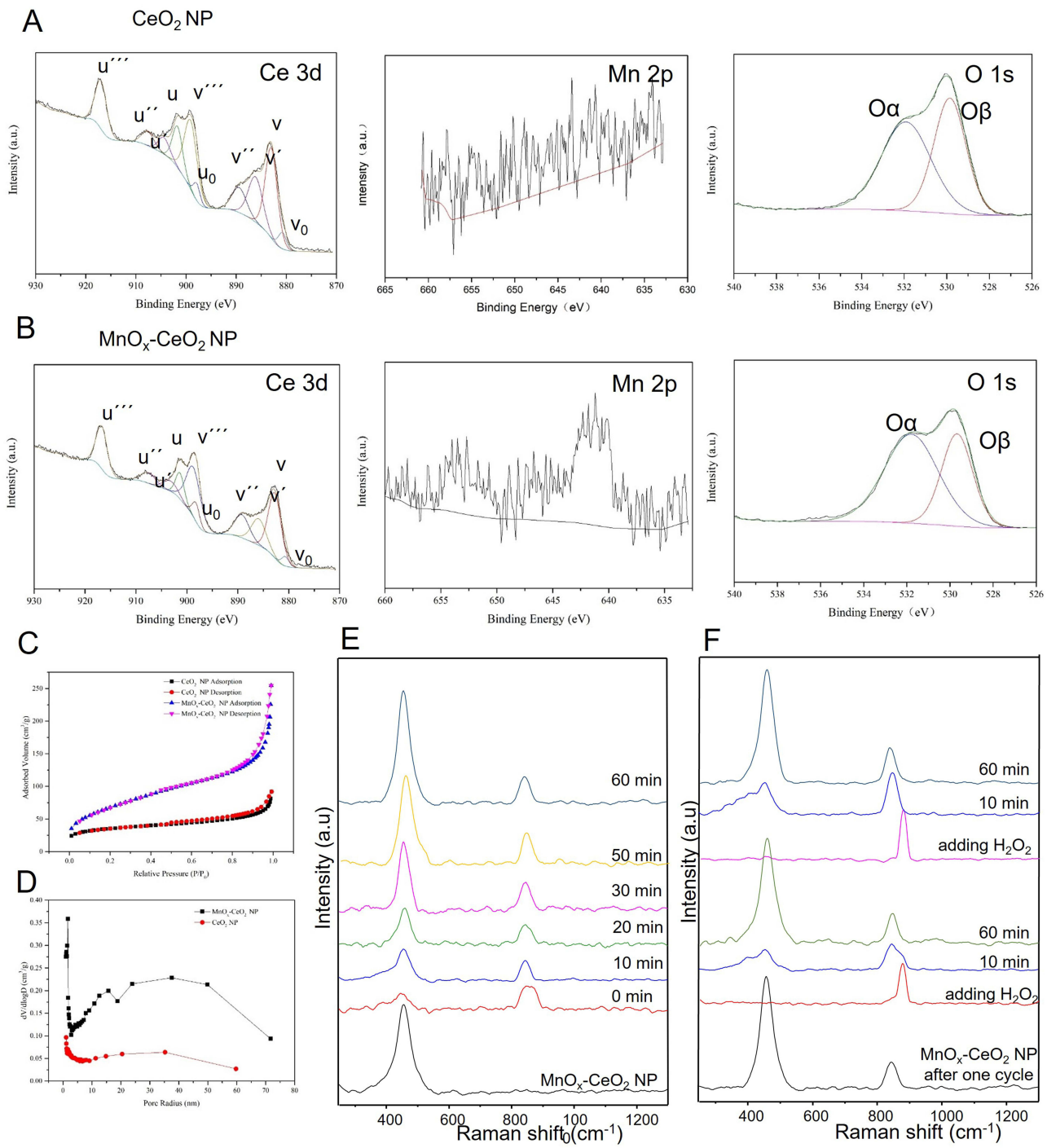

Figure 3 The valence state, specific surface area and oxygen vacancy of CeO_2 NPs and MnO_x-CeO_2 NPs. (**A**) XPS spectra of CeO_2 NPs, (**B**) XPS spectra of MnO_x-CeO_2 NPs, (**C**) The nitrogen adsorption/desorption isotherm of CeO_2 NPs and MnO_x-CeO_2 NPs, (**D**) BJH pore size distribution of CeO_2 NPs and MnO_x-CeO_2 NPs, (**E**) In situ Raman spectra of MnO_x-CeO_2 NPs when it was reacted with H_2O_2, (**F**) In situ Raman spectra of the cyclic reaction of MnO_x-CeO_2 NPs with H_2O_2.

and AST mainly exist in hepatocytes and they can be detected in the peripheral blood only in the circumstances of the hepatocytes are damaged and ruptured. The higher level of ALT and AST indicates more severe hepatocytes damage. As shown in Figures 4C and S3, the serum AST and ALT level in the MnO_x-CeO_2 NP groups was within the normal range and not significant different from the control. The result of the routine blood analysis was shown in Figure 4D. The relevant data of leukocytes, lymphocytes, monocytes, and neutrophils (WBC, Lymph#, Lymph%, Mon#, Mon%, Gran#, Gran%), erythrocyte-related data (RBC, HGB, HCT, MCV, MCH, MCHC and RDW) and platelet-related data (PLT,

Table 1 The Parameters of Valence State and Mesoporous Structure in CeO_2 NPs and MnO_x-CeO_2 NPs

	[Oα] (%)	[Oβ] (%)	[Ce^{3+}] (%)	S_{BET} (m^2/g)	Total Pore Volume (cm^3/g)	Pore Radius (nm)
CeO_2 NP	54.3	45.7	23.7	117.68	0.115	38.89
MnO_x-CeO_2 NP	62.5	37.5	21.4	245.42	0.363	36.78

MPV, PDW, PCT) in the blood of the MnO_x-CeO_2 NPs group were not significantly different from the control group ($P > 0.05$), which indicated that the i.v. injection of MnO_x-CeO_2 NPs did not cause any inflammatory response or significantly affect the cells in the blood. There were also no acute or chronic pathological changes in the organ sections of mice (Figure 4E). Therefore, MnO_x-CeO_2 NPs exhibited good biocompatibility after being intravenously injected in the mice.

Biodistribution of the MnO_x-CeO_2 NPs

As Mn is widely and naturally distributed in the body, especially liver, kidney and muscle, the biodistribution of MnO_x-CeO_2 NPs in mice after intravenous injection was evaluated by detecting the Ce levels in each organ via ICP-MS. As shown in Figure S4, the nanoparticles mainly distributed in the spleen and liver, in which the concentration of Ce was about 1 $mg \cdot kg^{-1}$, which was much higher than that in the lung, kidney, blood and heart. Therefore, MnO_x-CeO_2 NPs exhibited a passive liver-targeting effect after intravenous injection.

Anti-HIRI Effect of MnO_x-CeO_2 NPs

As the MnO_x-CeO_2 NPs showed much better anti-oxidant effect in the in vitro studies, the anti-HIRI effect of MnO_x-CeO_2 NPs was further evaluated in a mice HIRI model. As shown in Figure 5, the ALT and AST level in the serum of the HIRI group was significantly higher than that in the sham group ($P<0.05$), indicating the liver cells were damaged during the operation and the mouse HIRI model was successfully established. The ALT level in the MnO_x-CeO_2 NP group (0.50 $mg \cdot kg^{-1}$ and 1.00 $mg \cdot kg^{-1}$) was significantly lower than that in the HIRI group ($P<0.05$) and the AST level in the 1.00 $mg \cdot kg^{-1}$ MnO_x-CeO_2 NP group was significantly lower than that in the HIRI group ($P<0.05$), which indicated that MnO_x-CeO_2 NPs could significantly alleviate the liver damage caused by ischemia-reperfusion. MDA is the final product of lipid metabolism and the marker for lipid peroxidation, while SOD is a major intracellular antioxidant enzyme that catalyzes the conversion of superoxide into hydrogen peroxide and oxygen. The MDA level in liver tissue of the HIRI group was significantly higher than that of the sham group, the SOD level in the HIRI group was significantly lower than that of the sham group ($P<0.05$), which was consistent with the ALT/AST results. When pretreated with 1 $mg \cdot kg^{-1}$ MnO_x-CeO_2 NPs, MDA level was significantly decreased, SOD level was significantly increased, and they were not significantly different from the Sham group. While, 0.50 $mg \cdot kg^{-1}$ MnO_x-CeO_2 NPs could only significantly reduce the MDA level. Therefore, MnO_x-CeO_2 NPs could alleviate the cell damage caused by oxidative stresses. In the H&E staining of the liver tissue sections, small and irregular hepatocyte nuclei, disintegrated hepatic cord, obvious vacuolar degeneration and local hemorrhage areas were observed in the HIRI group. In the Sham group, no congestion, tissue necrosis, vacuoles degeneration or other pathological changes were found. In the 0.50 $mg \cdot kg^{-1}$ MnO_x-CeO_2 NP group, only mild vacuolar degeneration was observed in the hepatocytes, the nuclei of hepatocytes and hepatic cords remained to be normal. While in the 1.00 $mg \cdot kg^{-1}$ MnO_x-CeO_2 NP group, no irregular hepatocyte nuclei, disintegrated hepatic cord, vacuolar degeneration or local hemorrhage areas could be observed. Therefore, MnO_x-CeO_2 NPs could significantly reduce the liver damage caused by HIRI. Manne et al found that intravenous administration of CeO_2 NPs (0.5 mg/kg) one hour before HIRI could significantly decrease the levels of ALT and LDH (markers of liver cell damage), macrophage inflammatory protein-2, myoglobin and plasminogen activator inhibitor-1 (inflammatory markers) in the serum and inhibit the necrosis of liver cells.[29] More and more evidence proved that CeO_2 NPs can rapidly remove excess ROS, reduce the necrosis of hepatocytes, inhibit the activation of Kupffer cells and monocyte macrophages, decrease the of pro-inflammatory cytokines, and thus reduce the adhesion, recruitment and infiltration of neutrophils, repolarize macrophages from M1 to M2 and ultimately inhibit the liver injury. Our results correlated well with the previous studies.[11,20,30,31]

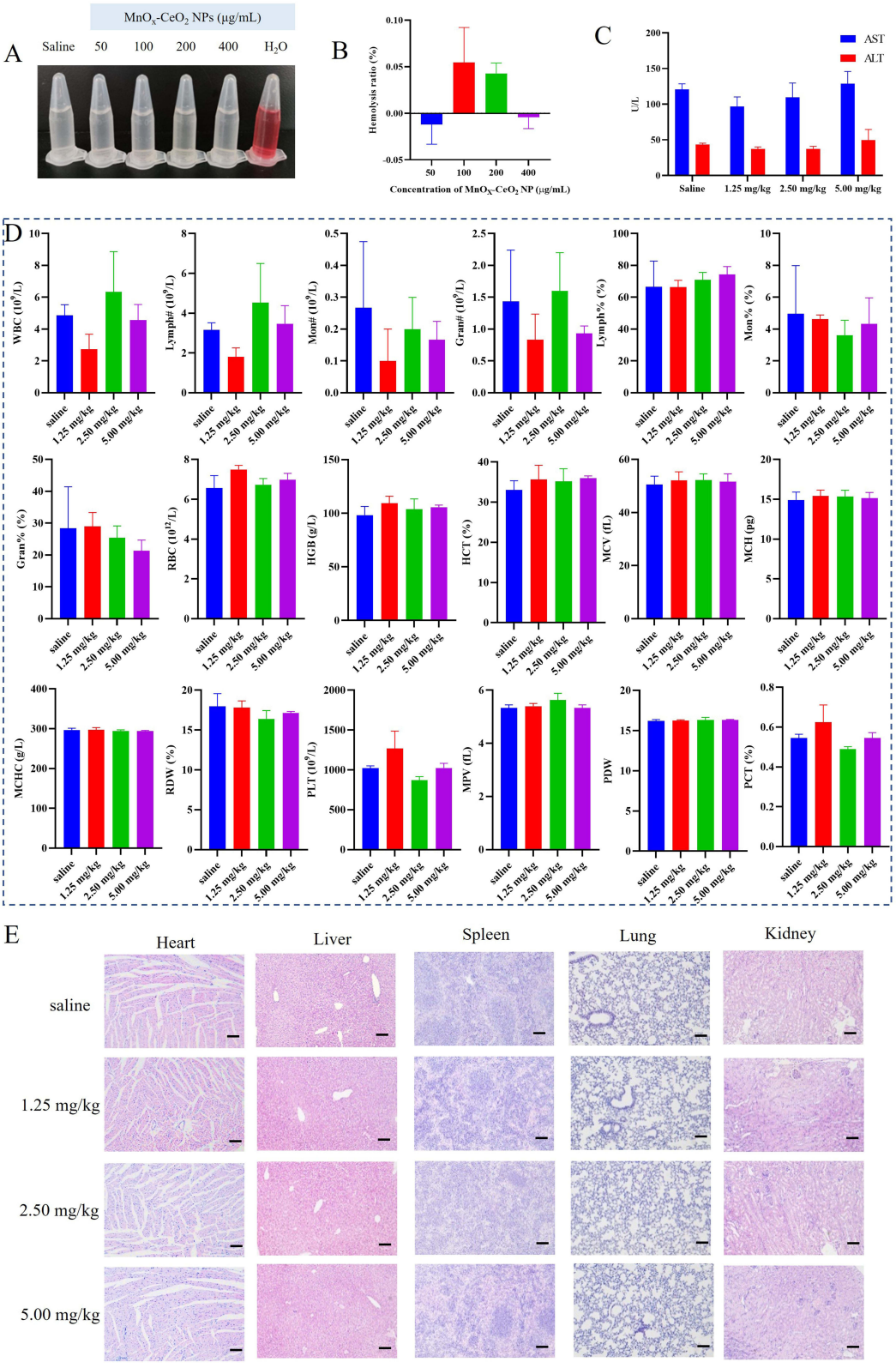

Figure 4 Biosafety of MnO_x-CeO_2 NPs. (**A**) Image of the hemolysis study, (**B**) Hemolysis rate, (**C**) The ALT and AST level in the serum 1 day after *i.v.* injection, (**D**) blood analysis 1 day after *i.v.* injection, (**E**) The H&E staining of different organ slides 1 day after *i.v.* injection.

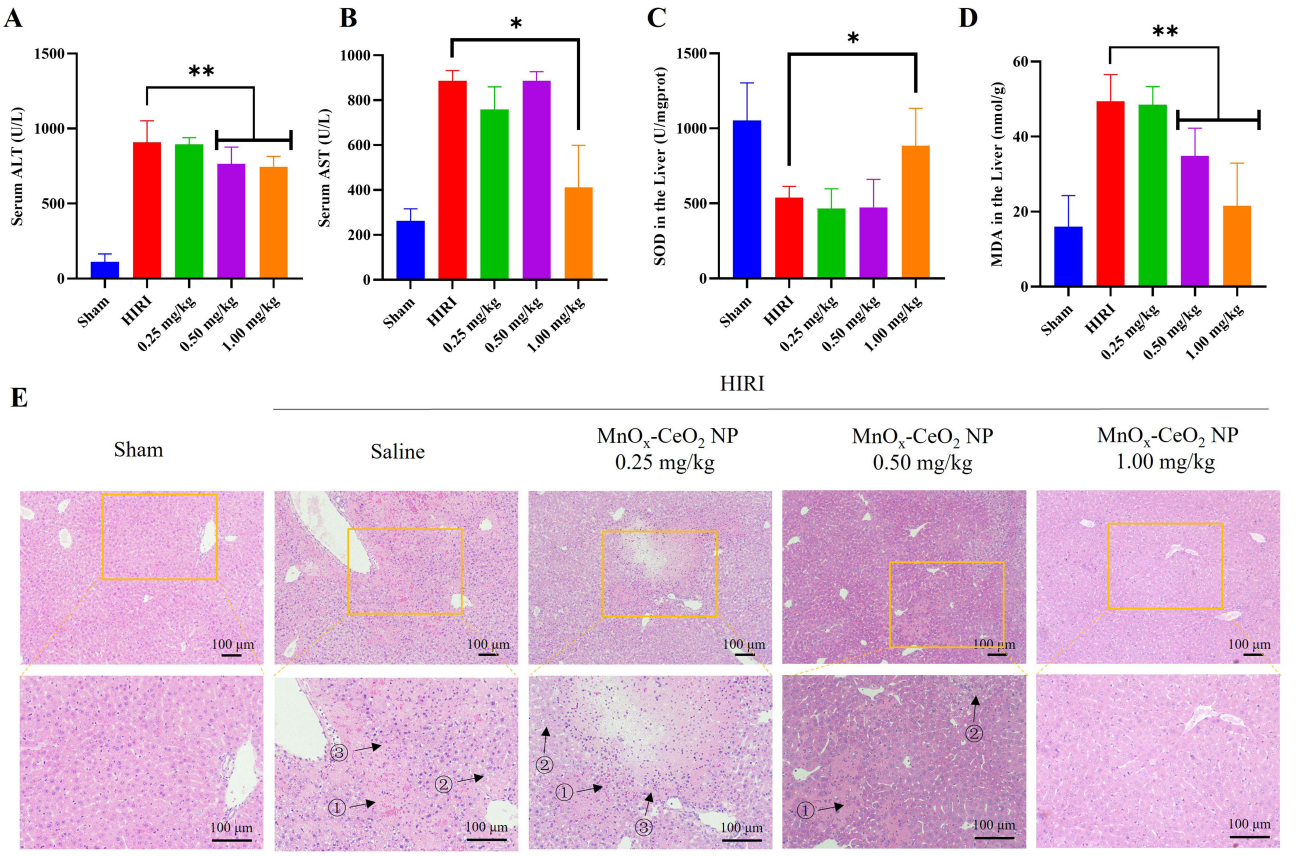

Figure 5 The in vivo anti-HIRI effect of MnO_x-CeO_2 NPs. (**A**) ALT level in the serum of different groups, (**B**) AST level in the serum of different groups, (**C**) MDA level in the liver of different groups, (**D**) SOD level in the liver of different groups, (**E**) H&E staining of liver tissue sections in different groups, ① cell necrosis with hepatic cord disintegration and hemorrhage, ② cytoplasmic vacuolar degeneration, ③ focal nuclear pyknosis. * denotes $P<0.05$, ** denotes $P<0.01$.

Conclusion

In this study, we assessed the application of MnO_x-CeO_2 NPs in the management of HIRI. The MnO_x-CeO_2 NPs with 4% Mn doping ratio exhibited the best anti-oxidant capability and the size of the nanoparticles was approximately 220 nm. After doping with Mn, the oxygen vacancy concentration and specific surface area were significantly increased, which was directly related to the elevated anti-oxidant effect in the EPR measurement. Besides, MnO_x-CeO_2 NPs exhibited no toxicity to BALB/C mice and it was enriched in the liver after intravenous injection. In the in vivo HIRI mice model, 1.00 $mg \cdot kg^{-1}$ MnO_x-CeO_2 NPs significantly reduced the ALT and AST level in the serum, decreased the MDA level, increased the SOD level in the liver and attenuated the pathological changes caused by the HIRI. As a result, MnO_x-CeO_2 NPs exhibits great potential as a novel pharmacotherapy in the management of HIRI.

Acknowledgments

We are grateful for the financial support from the Natural Science Foundation of Shaanxi Province (grant numbers 2021SF-118), the Project of Independent Innovative Experiment for Postgraduates in medicine in Xi'an Jiaotong University (grant number YJSCX-2018-005) and National Natural Science Foundation of China (grant numbers 81973409, 81903733, 81903320, 82204631).

Disclosure

The authors declare that they have no known competing financial interests or personal relationships that could have appeared to influence the work reported in this paper.

References

1. Cannistra M, Ruggiero M, Zullo A, et al. Hepatic ischemia reperfusion injury: a systematic review of literature and the role of current drugs and biomarkers. *Int J Surg*. 2016;33(Suppl 1):S57–70. doi:10.1016/j.ijsu.2016.05.050
2. McCord JM. Oxygen-derived free radicals in postischemic tissue injury. *N Engl J Med*. 1985;312(3):159–163. doi:10.1056/NEJM198501173120305
3. Jaeschke H, Smith CV, Mitchell JR. Reactive oxygen species during ischemia-reflow injury in isolated perfused rat liver. *J Clin Invest*. 1988;81(4):1240–1246. doi:10.1172/JCI113441
4. Monga SP. Lipid metabolic reprogramming in hepatic ischemia-reperfusion injury. *Nat Med*. 2018;24(1):6–7. doi:10.1038/nm.4468
5. Eltzschig HK, Eckle T. Ischemia and reperfusion-from mechanism to translation. *Nat Med*. 2011;17(11):1391–1401. doi:10.1038/nm.2507
6. Kyriakopoulos G, Valsami G, Tsalikidis C, Pitiakoudis M, Tsaroucha AK. Use of natural anti-oxidants in experimental animal models of hepatic ischemia-reperfusion injury. *Ann Med Surg*. 2020;60:592–599. doi:10.1016/j.amsu.2020.11.061
7. Vazirov RA, Sokovnin SY, Ilves VG. Antioxidant Properties of Cerium Dioxide Nanoparticles. *Phys Chem Aspects Study Clusters Nanostruct Nanomater*. 2018;10:196–203. doi:10.26456/pcascnn/2018.10.196
8. He LZ, Huang GN, Liu HX, Sang CC, Liu XX, Chen TF. Highly bioactive zeolitic imidazolate framework-8-capped nanotherapeutics for efficient reversal of reperfusion-induced injury in ischemic stroke. *Science Advances*. 2020;6(12):45. doi:10.1126/sciadv.aay9751
9. Kwon HJ, Kim D, Seo K, et al. Ceria Nanoparticle Systems for Selective Scavenging of Mitochondrial, Intracellular, and Extracellular Reactive Oxygen Species in Parkinson's Disease. *Angewandte Chemie-International Edition*. 2018;57(30):9408–9412. doi:10.1002/anie.201805052
10. Zhang DY, Liu HK, Li CY, et al. Ceria Nanozymes with Preferential Renal Uptake for Acute Kidney Injury Alleviation. *ACS Appl Mater Interfaces*. 2020;12(51):56830–56838. doi:10.1021/acsami.0c17579
11. Ni D, Wei H, Chen W, et al. Ceria Nanoparticles Meet Hepatic Ischemia-Reperfusion Injury: the Perfect Imperfection. *Adv Mater*. 2019;31(40):e1902956. doi:10.1002/adma.201902956
12. Yang W, Wang X, Song S, Zhang H. Syntheses and Applications of Noble-Metal-free CeO2-Based Mixed-Oxide Nanocatalysts. *Chem*. 2019;5(7):1743–1774. doi:10.1016/j.chempr.2019.04.009
13. Han SI, Lee SW, Cho MG, et al. Epitaxially Strained CeO2/Mn3O4 Nanocrystals as an Enhanced Antioxidant for Radioprotection. *Adv Mater*. 2020;32(31):35. doi:10.1002/adma.202001566
14. Soh M, Kang DW, Jeong HG, et al. Ceria-Zirconia Nanoparticles as an Enhanced Multi-Antioxidant for Sepsis Treatment. *Angew Chem Int Ed Engl*. 2017;56(38):11399–11403. doi:10.1002/anie.201704904
15. Zou S, Guo F, Wu L, et al. One-pot synthesis of cerium and praseodymium co-doped carbon quantum dots as enhanced antioxidant for hydroxyl radical scavenging. *Nanotechnology*. 2020;31(16):165101. doi:10.1088/1361-6528/ab5b40
16. Zhen J, Wang X, Liu D, et al. Co(3)O(4)@CeO(2) core@shell cubes: designed synthesis and optimization of catalytic properties. *Chemistry*. 2014;20(15):4469–4473. doi:10.1002/chem.201304109
17. Shi J, Yu W, Xu L, et al. Bioinspired Nanosponge for Salvaging Ischemic Stroke via Free Radical Scavenging and Self-Adapted Oxygen Regulating. *Nano Lett*. 2020;20(1):780–789. doi:10.1021/acs.nanolett.9b04974
18. Xue Y, Luan QF, Yang D, Yao X, Zhou KB. Direct Evidence for Hydroxyl Radical Scavenging Activity of Cerium Oxide Nanoparticles. *J Phys Chem C*. 2011;115(11):4433–4438. doi:10.1021/jp109819u
19. Mitchell KJ, Goodsell JL, Russell-Webster B, et al. Expansion of the Family of Molecular Nanoparticles of Cerium Dioxide and Their Catalytic Scavenging of Hydroxyl Radicals. *Inorg Chem*. 2021;60(3):1641–1653. doi:10.1021/acs.inorgchem.0c03133
20. Long Y, Wei H, Li J, et al. Prevention of Hepatic Ischemia-Reperfusion Injury by Carbohydrate-Derived Nanoantioxidants. *Nano Lett*. 2020;20(9):6510–6519. doi:10.1021/acs.nanolett.0c02248
21. Lim H, Kim TY, Kim SY, et al. The Protective Effects of Dexmedetomidine Preconditioning on Hepatic Ischemia/Reperfusion Injury in Rats. *Transplant Proc*. 2021;53(1):427–435. doi:10.1016/j.transproceed.2020.10.014
22. Narayana BL, Mukri BD, Ghosal P, Subrahmanyam C. Mn Ion substituted CeO2 Nano spheres for Low Temperature CO Oxidation: the Promoting Effect of Mn Ions. *Chemistryselect*. 2016;1(12):3150–3158. doi:10.1002/slct.201600152
23. Jia J, Zhang T, Chi J, et al. Neuroprotective Effect of CeO2@PAA-LXW7 Against H2O2-Induced Cytotoxicity in NGF-Differentiated PC12 Cells. *Neurochem Res*. 2018;43(7):1439–1453. doi:10.1007/s11064-018-2559-y
24. Lin X, Zhao SF, Fu LL, Luo YM, Zhu RL, Liu ZG. Synthesis of Co-N-C grafted on well-dispersed MnOx-CeO2 hollow mesoporous sphere with efficient catalytic performance. *Mol Catal*. 2017;437:18–25. doi:10.1016/j.mcat.2017.04.026
25. Dosa M, Piumetti M, Bensaid S, et al. Novel Mn–Cu-Containing CeO2 Nanopolyhedra for the Oxidation of CO and Diesel Soot: effect of Dopants on the Nanostructure and Catalytic Activity. *Catal Letters*. 2017;148(1):298–311. doi:10.1007/s10562-017-2226-y
26. Sudarsanam P, Hillary B, Mallesham B, et al. Designing CuOx Nanoparticle-Decorated CeO2 Nanocubes for Catalytic Soot Oxidation: role of the Nanointerface in the Catalytic Performance of Heterostructured Nanomaterials. *Langmuir*. 2016;32(9):2208–2215. doi:10.1021/acs.langmuir.5b04590
27. Sartoretti E, Novara C, Giorgis F, et al. In situ Raman analyses of the soot oxidation reaction over nanostructured ceria-based catalysts. *Sci Rep*. 2019;9(1):3875. doi:10.1038/s41598-019-39105-5
28. Chen W, Xie J, Li X, Li L. Oxygen vacancies and Lewis sites activating O3/H2O2 at wide pH range via surface electron transfer over CeOx@SiO2 for nitrobenzene mineralization. *J Hazard Mater*. 2021;406:124766. doi:10.1016/j.jhazmat.2020.124766
29. Córdoba-Jover B, Arce-Cerezo A, Ribera J, et al. Cerium oxide nanoparticles improve liver regeneration after Acetaminophen-induced liver injury and partial hepatectomy in rats. *J Nanobiotechnology*. 2019;17(1):112. doi:10.1186/s12951-019-0544-5
30. Casals G, Perramón M, Casals E, et al. Cerium Oxide Nanoparticles: a New Therapeutic Tool in Liver Diseases. *Antioxidants*. 2021;10(5):654. doi:10.3390/antiox10050660
31. Del Turco S, Cappello V, Tapeinos C, et al. Cerium oxide nanoparticles administration during machine perfusion of discarded human livers: a pilot study. *Liver Transpl*. 2022;28(7):1173–1185. doi:10.1002/lt.26421